

DiGAN: Diffusion-Guided Attention Network for Early Alzheimer’s Disease Detection

Maxx Richard Rahman^{1,2}, Mostafa Hammouda^{1,2}, Wolfgang Maass^{1,2}

¹German Research Center for Artificial Intelligence (DFKI), Germany

²Saarland University, Germany

Abstract

Early diagnosis of Alzheimer’s disease (AD) remains a major challenge due to the subtle and temporally irregular progression of structural brain changes in the prodromal stages. Existing deep learning approaches require large longitudinal datasets and often fail to model the temporal continuity and modality irregularities inherent in real-world clinical data. To address these limitations, we propose the Diffusion-Guided Attention Network (DiGAN), which integrates latent diffusion modelling with attention-guided convolutional network. The diffusion model synthesizes realistic longitudinal neuroimaging trajectories from limited training data, enriching temporal context and improving robustness to unevenly spaced visits. The attention-convolutional layer then captures discriminative structural-temporal patterns that distinguish cognitively normal subjects from those with mild cognitive impairment and subjective cognitive decline. Experiments on synthetic and ADNI datasets demonstrate that DiGAN outperforms existing state-of-the-art baselines, showing its potential for early-stage AD detection.

Introduction

Alzheimer’s disease (AD) is the most prevalent neurodegenerative disorder, accounting for 60–80% of dementia cases worldwide (Alzheimer 2024). It affects over 50 million individuals globally, with cases projected to triple by 2050 (WHO 2017). The resulting cognitive and functional decline imposes immense socioeconomic and healthcare burdens. Therefore, early detection of prodromal AD is important for enabling preventive interventions, guiding treatment decisions, and improving patient outcomes (Di Meco and Vassar 2021). However, reliable identification of early-stage AD remains a challenge due to several factors (Zhang et al. 2024a): (i) subtle morphological changes in the brain precede clinical symptoms by years, (ii) disease trajectories are highly heterogeneous across individuals, and (iii) longitudinal neuroimaging data are limited, irregular, and often incomplete.

Recent advances in deep learning have improved AD characterization by identifying structural and temporal biomarkers from neuroimaging data. Ensemble-based approaches like LSCP (Zhao et al. 2019) and SUOD (Zhao

et al. 2021) have improved detection robustness, while probabilistic models such as GP (Hyun et al. 2016) has been explored for anomaly detection in clinical data. Attention-based model like SACNN (Rahman et al. 2024) exploits structural-temporal dependencies in longitudinal data. Despite its effectiveness, existing models share key limitations: (i) they require large amounts of longitudinal training data to generalize effectively, which is an unrealistic assumption in the healthcare domain where follow-up data are often sparse and irregular; and (ii) they are unable to synthesize intermediate disease states reflecting continuous progression. These limitations motivate the development of models capable of generating realistic temporal trajectories and learning discriminative representations from limited and irregular clinical data.

To overcome these limitations, we propose the Diffusion-Guided Attention Network (DiGAN), a generative-discriminative architecture designed for early Alzheimer’s disease detection. DiGAN integrates a latent diffusion model with an attention-based convolutional network to synthesize realistic longitudinal profiles and improve temporal modeling. The diffusion component generates additional neuroimaging trajectories that mimic real-world disease progression, while the attention-convolutional encoder captures discriminative structural-temporal representations for early AD detection. The key contributions are summarized as follows:

- We introduce DiGAN that fuses latent diffusion modeling with attention-based convolution for early AD detection from longitudinal neuroimaging data.
- We demonstrate the effectiveness of DiGAN compared to existing state-of-the-art methods on both the synthetic and ADNI datasets.

Preliminaries

The objective is to detect prodromal AD by modeling temporal progression within longitudinal neuroimaging profiles. Each subject i is represented by a sequence of structural MRI-derived biomarkers across baseline and follow-up visits, denoted as $\mathbf{X}_i = \{\mathbf{x}_{i,1}, \mathbf{x}_{i,2}, \dots, \mathbf{x}_{i,n_i}\}$, $\mathbf{x}_{i,t} \in \mathbb{R}^p$, where n_i is the number of available visits and p is the dimensionality of the biomarker feature space. Each feature vector $\mathbf{x}_{i,t}$ includes regional brain volumes, white matter hyperin-

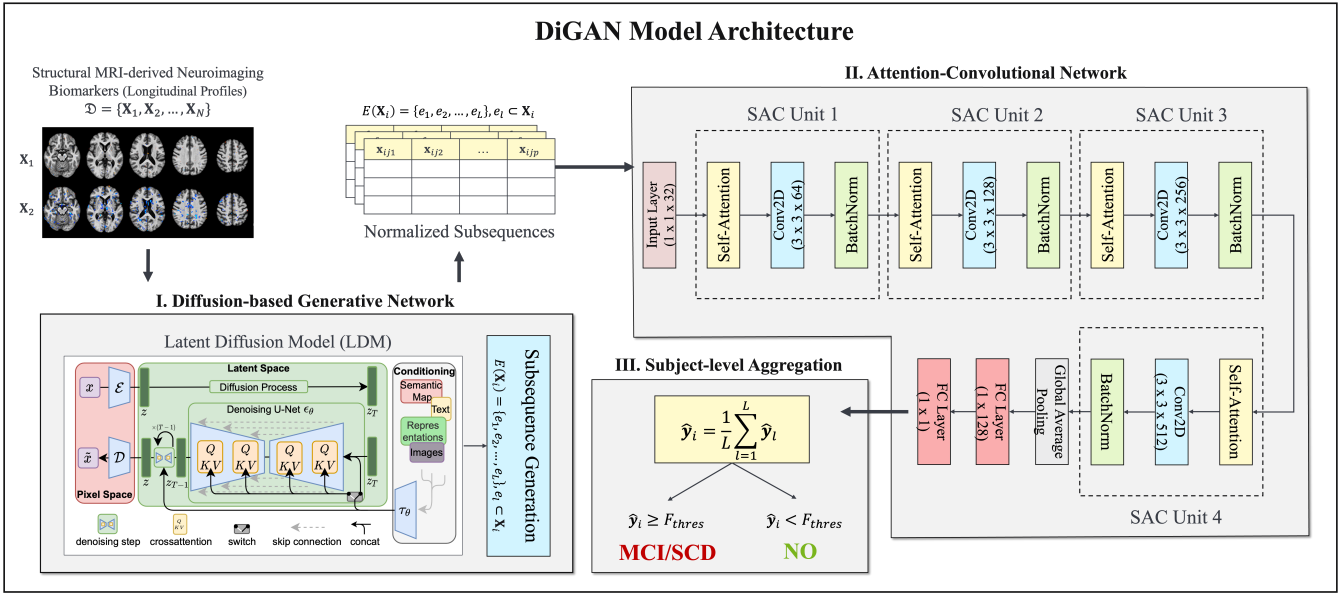


Figure 1: Overview of the DiGAN architecture comprising (i) a diffusion process for synthesizing neuroimaging profiles, (ii) an attention-convolutional network for extracting structural–temporal embeddings, and (iii) a subject-level aggregation for AD identification.

tensities, perivascular spaces, etc. Each subject is assigned a diagnostic label y_i , indicating cognitively normal (NO), subjective cognitive decline (SCD), mild cognitive impairment (MCI), and Alzheimer’s disease (AD). The task is to learn a discriminative function $f_\theta : \mathbf{X}_i \mapsto y_i$ that captures both structural and temporal dependencies across visits (from baseline), thereby modeling disease progression and identifying subjects at different stages of cognitive decline.

DiGAN Architecture

As shown in Fig. 1, the DiGAN consists of three main components: i) Diffusion-based generative network, ii) Attention-convolutional network, and iii) Subject-level aggregation unit.

Diffusion-based Generative Network

We generate neuroimaging profiles that mimic real-world progressions by following the latent diffusion framework (Rombach et al. 2022). The forward process gradually perturbs a clean MRI-derived feature vector $\mathbf{x}_{i,t}$ into a noisy latent variable \mathbf{z}_t through a sequence of Gaussian transitions: $\mathbf{z}_0 = \mathbf{x}_{i,t}, \mathbf{z}_t = \sqrt{\alpha_t} \mathbf{z}_{t-1} + \sqrt{1 - \alpha_t} \epsilon_t, \epsilon_t \sim \mathcal{N}(0, I)$, where $\{\alpha_t\}_{t=1}^T$ defines the variance schedule controlling the noise magnitude. A denoising network $\mathcal{D}_\theta(\mathbf{z}_t, t)$ learns the reverse process, progressively reconstructing clean representations $\hat{\mathbf{x}}_{i,t}$ by minimizing the mean squared error between the true and predicted noise, which corresponds to maximizing a variational lower bound on $\log p(\mathbf{x})$.

When the synthetic longitudinal profile $\hat{\mathbf{X}}_i = \{\hat{\mathbf{x}}_{i,1}, \dots, \hat{\mathbf{x}}_{i,n_i}\}$ is generated, we apply a subsequence extraction function to handle the irregular and variable sequence lengths. The set of subsequences derived from each

profile is defined as $E(\hat{\mathbf{X}}_i) = \{e_1, e_2, \dots, e_L\}, e_l \subset \hat{\mathbf{X}}_i$, where each subsequence e_l corresponds to a contiguous temporal window of length L . All subsequences are normalized across samples to ensure consistency in feature scaling.

Attention-Convolutional Network

Each normalized subsequence is fed into an attention-convolutional network composed of m stacked Self-Attention Convolution (SAC) units. The purpose is to extract structural–temporal embeddings that capture both global progression trends and local variations in biomarker dynamics. In the j^{th} SAC unit (Rahman et al. 2024), the input sequence representation $H^{(j-1)} \in \mathbb{R}^{L \times C_{j-1}}$ (where C_{j-1} denotes the number of input channels) is processed through the following operations:

1. Self-Attention Layer: Temporal dependencies across samples are modeled via a scaled dot-product attention mechanism. The attention matrix is computed as $\mathcal{A} = \text{softmax}\left(\frac{QK^\top}{\sqrt{d_a}}\right)$, and the attention-weighted output is $H_a = \mathcal{A}V$. This allows the network to emphasize clinically relevant time points while capturing long-range dependencies across visits.

2. Convolutional Layer: The attention-weighted representation H_a is subsequently processed by a two-dimensional convolution operating over both time and feature dimensions $H_{\text{conv}}^{(j)} = \sigma(W^{(j)} * H_a + b^{(j)})$, where $W^{(j)}$ and $b^{(j)}$ denote the convolutional kernels and bias, respectively, and $\sigma(\cdot)$ represents a non-linear activation function. This refines feature interactions by capturing localized structural–temporal dependencies among brain biomarkers.

3. Batch Normalization and Output: To stabilize optimization and improve generalization, batch normalization is applied channel-wise $H_{\text{BN}}^{(j)} = \frac{H_{\text{conv}}^{(j)} - \mu}{\sqrt{\sigma^2 + \epsilon}} \gamma + \beta$, where μ and σ^2 denote the batch mean and variance, and γ, β are learnable scaling and shift parameters. The resulting normalized features are propagated to the next SAC unit. After the final unit, the representation is flattened into a vector h , which is passed through a fully connected layer to produce a subsequence-level logit $l_{e_\ell} = w^\top h + b$, followed by a sigmoid activation $p_{e_\ell} = \sigma(l_{e_\ell})$, representing the probability that subsequence e_ℓ corresponds to an impaired cognitive state.

Subject-Level Aggregation

For each subject, the attention-convolutional network produces a set of subsequence-level probabilities $\{p_{e_\ell}\}_{\ell=1}^L$, where each p_{e_ℓ} reflects the likelihood that the corresponding temporal window $e_\ell \subset E(\hat{\mathbf{X}}_i)$ indicates cognitive impairment. To derive a subject-level decision, these probabilities are aggregated using a clinically motivated maximum-pooling rule $p_i = \max_\ell p_{e_\ell}$. A subject is classified as impaired if $p_i \geq F_{\text{thres}}$, (F_{thres} : predefined decision threshold). This aggregation reflects the clinical rationale that the presence of neurodegenerative evidence in any temporal segment of the longitudinal profile is sufficient to indicate elevated risk.

Model Training and Optimization

The diffusion model is optimized to reconstruct clean MRI-derived representations by minimizing the standard diffusion objective $\mathcal{L}_{\text{diff}} = \mathbb{E}_{t, \mathbf{x}, \epsilon} [\|\epsilon - \mathcal{D}_\theta(\sqrt{\alpha_t} \mathbf{x} + \sqrt{1 - \alpha_t} \epsilon, t)\|_2^2]$. This objective corresponds to optimizing a variational lower bound on the data likelihood. The attention-convolutional network is trained using a binary cross-entropy loss augmented with an adversarial rate regularization term to mitigate class imbalance and improve specificity. Given a batch of subsequences $\{e_b\}_{b=1}^B$ with corresponding labels $y_b \in \{0, 1\}$ and predicted probabilities p_b , the loss function is defined as $\mathcal{L}_{\text{cls}} = -\frac{1}{B} \sum_{b=1}^B [y_b \log p_b + (1 - y_b) \log(1 - p_b)] + \lambda \left(\frac{\sum_{b: y_b=1} p_b}{\sum_{b: y_b=0} p_b} \right)$, where λ controls the trade-off between classification accuracy and class-wise regularization. The second term penalizes disproportionate positive-to-negative prediction ratios, promoting higher specificity and robust discrimination under imbalanced data conditions. The overall training objective combines the diffusion reconstruction loss and the classification loss: $\mathcal{L} = \mathcal{L}_{\text{diff}} + \beta \mathcal{L}_{\text{cls}}$, where β balances generative and discriminative learning.

Experiments

Datasets

Synthetic dataset. We use a synthetic longitudinal dataset derived from the DELCODE study (Jessen et al. 2018), to simulate realistic neuroimaging trajectories observed in early-stage AD (Table 1). These profiles were generated by modeling intrasubject trajectories using a 2nd polynomial

Table 1: Data statistics across different diagnostic groups.

Datasets	Statistics (Male/Female)				Total	
	NO	MCI	SCD	AD		
Synthetic	# subjects	101/139	96/88	208/180	33/37	438/444
	# visits	336/439	207/156	560/508	46/56	1149/1159
ADNI	# subjects	97/158	36/60	-	186/150	319/368
	# visits	158/318	65/117	-	291/236	514/671

function fitted to real distributions, followed by the addition of low-variance Gaussian noise to simulate intersubject variability and measurement uncertainty. Each profile comprises volumetric measures of cortical and subcortical regions, including the entorhinal cortex, parahippocampal gyrus, precuneus, posterior cingulate, and temporal lobes, as well as white matter hyperintensities (WMH) in the frontal and parietal lobes, perivascular spaces (PVS) in the basal ganglia and centrum semiovale.

ADNI. (Petersen et al. 2010) A longitudinal study widely used for Alzheimer’s disease research. Subjects with at least two MRI sessions were included. Compared to the synthetic dataset, ADNI exhibits higher inter-subject variability and more pronounced class imbalance, providing a challenging real-world testbed for evaluating the model generalizability.

Experimental Settings

Tasks. Since this work focuses on early AD detection, we conduct classification tasks targeting the prodromal stages of impairment: NO vs. MCI and NO vs. SCD. We consider $n_i \in \{2, 3, 4\}$ to reflect subjects with different numbers of visits. Evaluation metrics include accuracy, sensitivity, specificity, precision, F1-score and area under the ROC.

Baseline Methods. We compare DiGAN against state-of-the-art linear method (ALASCA (Truter et al. 2022)), generative models (TVAE (Zhang et al. 2024b), AnoGAN (Schlegl et al. 2017)), probabilistic-kernel model (GP (Hyun et al. 2016)), and ensemble-based methods (LSCP (Zhao et al. 2019), SUOD (Zhao et al. 2021), IsoForest (Liu, Ting, and Zhou 2008)) for longitudinal anomaly detection.

Results

Synthetic Dataset Evaluation

To assess the quality of the synthetic profiles by the diffusion model, we perform a comparison analysis between the synthetic and real distributions. As shown in Fig. 2, the probability density curves of different parameters (ADNI) show a strong overlap, with only minor deviations observed in extreme regions of the distributions. Quantitatively, similarity metrics remain consistently low, indicating high fidelity between these measurements. The differences in first- and higher-order moments ($\Delta\mu, \Delta\sigma$, skewness, and kurtosis) are within acceptable limits across most parameters, confirming that the generative process preserves anatomical variability. Fig. 5 shows that the differential correlation heatmap and the PCA visualisation corroborate these findings by showing

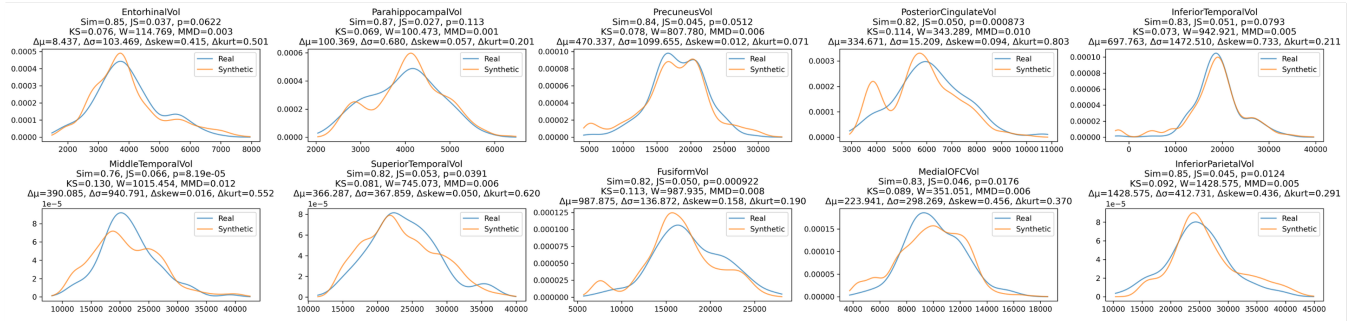


Figure 2: Comparison between real and synthetic ADNI data distributions of different parameters.

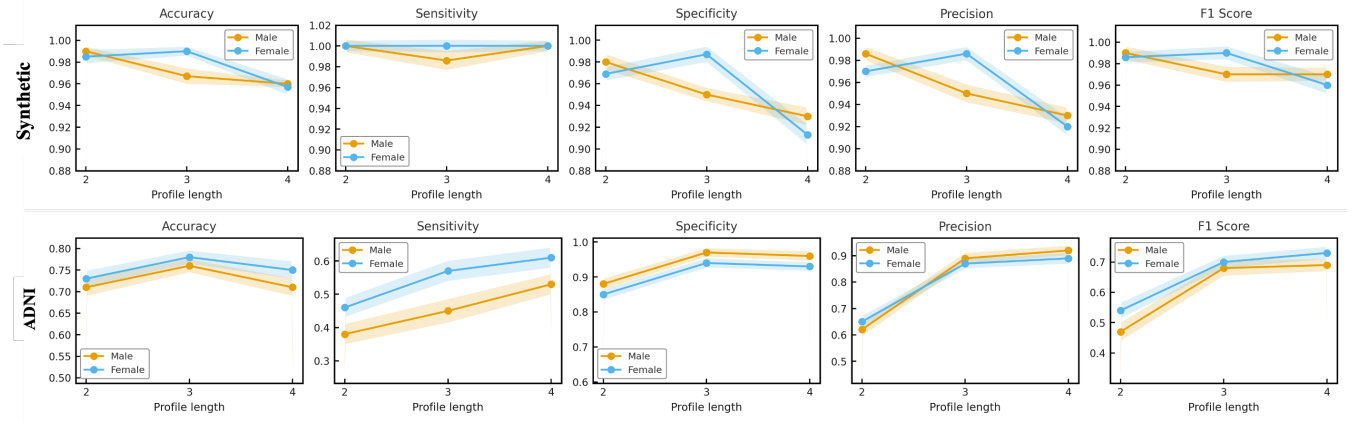


Figure 3: Performance of DiGAN for NO vs. MCI across profile lengths of 2, 3, and 4 visits.

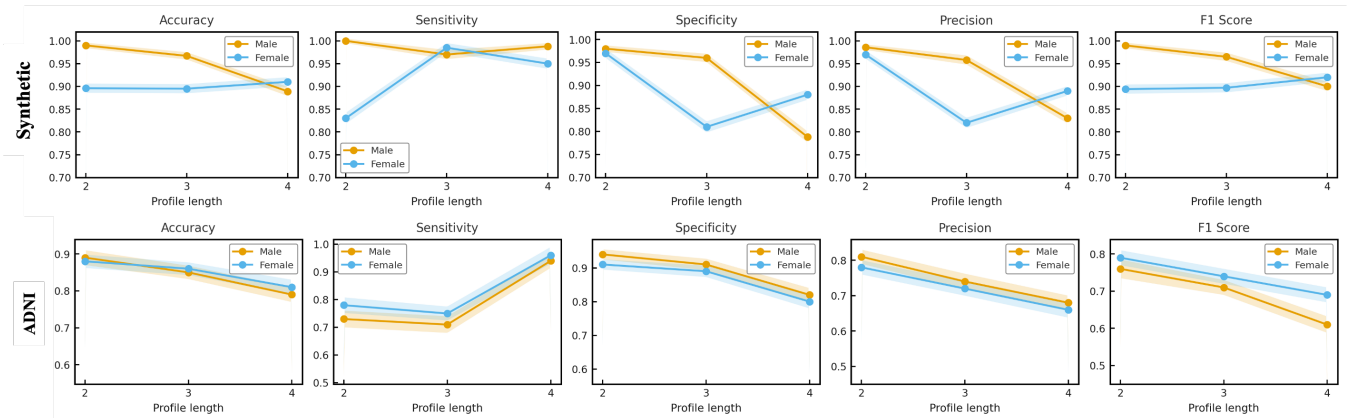


Figure 4: Performance of DiGAN for NO vs. SCD (synthetic) and NO vs. AD (ADNI) across profile lengths of 2, 3, and 4 visits.

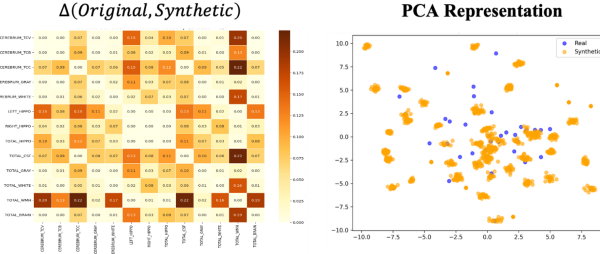


Figure 5: The differential correlation heatmap (left) and a PCA projection (right), showing substantial overlap between synthetic and real profiles.

substantial overlap in the latent space, implying that the synthetic data accurately captures the intrinsic variance structure of the real data.

NO vs. MCI Performance

Fig. 3 shows the classification performance of DiGAN for distinguishing cognitively normal from subjects with mild cognitive impairment. In the synthetic dataset, DiGAN achieves accuracy above 0.96 and sensitivities exceeding 0.99 for both male and female subjects. While performance remains stable across 2-4 longitudinal visits, a minor decline in specificity is observed for longer sequences in males, potentially due to reduced sample diversity. In contrast, the ADNI dataset, which contains greater inter-subject and acquisition variability, shows a more gradual improvement with increased temporal context: accuracy rises from 0.70 (2 visits) to 0.77 (3 visits), accompanied by similar gains in sensitivity and F1-score. This improvement demonstrates the model’s ability to leverage temporal continuity in longitudinal profiles for improved discrimination of subtle cognitive decline. In addition, Table 2 shows that DiGAN achieves an overall accuracy of 0.948 (synthetic) and 0.710 (ADNI), outperforming all baseline models.

NO vs. SCD and NO vs. AD Performance

Fig. 4 shows the classification performance of DiGAN for distinguishing cognitively normal individuals from those with subjective cognitive decline (synthetic) and from Alzheimer’s disease patients (ADNI). Distinguishing NO from SCD remains inherently challenging due to the subtle and self-reported nature of cognitive symptoms. Nevertheless, DiGAN achieves strong discrimination, achieving accuracy above 0.90 and F1-score exceeding 0.92 across most profile lengths. For male subjects, accuracy peaks around three visits with values near 0.94, and female subjects maintain comparable or slightly higher sensitivity, suggesting better generalization across profiles. In the ADNI dataset, where NO is distinguished with clinically diagnosed AD, DiGAN shows clear separability, achieving accuracy above 0.85 and sensitivity exceeding 0.95. As profile length increases from 2 to 4 visits, sensitivity improves consistently, substantiating the model’s ability to exploit longitudinal dynamics. Female subjects show marginally higher sensitivity and F1-scores, indicating that DiGAN effectively cap-

tures nuanced temporal biomarkers associated with early neurodegeneration.

Precision-Recall and ROC Analysis

Fig. 7 presents the ROC and precision–recall (PR) curves comparing DiGAN with baseline methods on the synthetic dataset for NO vs. MCI (male subjects). DiGAN consistently outperforms all state-of-the-art models, with the ROC curve indicating good discrimination between classes even under high specificity constraints. In the PR analysis, DiGAN achieves substantially higher average precision across all recall levels, maintaining stable performance in high-recall regions where baselines degrade rapidly. This robustness indicates that the diffusion-guided representation effectively captures subtle structural and temporal deviations associated with early cognitive decline. Among baselines, GP and TVAE perform moderately well but exhibit trade-offs between precision and recall. DiGAN’s advantage arises from the integration of the diffusion process, which enriches the latent space by reconstructing intermediate neuroanatomical trajectories, and the attention mechanism, which selectively amplifies clinically relevant temporal dependencies.

Embedding Maps from SAC Units

To better understand the representational dynamics within the DiGAN, we visualize the intermediate embedding maps generated by SAC units on the ADNI dataset, as shown in Fig. 6. The early SAC units (SAC 1 and SAC 2) exhibit diffuse and low-intensity activation patterns, indicating that the network captures broad, non-discriminative features common to both cognitively normal and mildly impaired subjects. In contrast, deeper SAC units (SAC 3 and SAC 4) show increasingly structured and high-intensity activations, corresponding to more localized and discriminative representations of disease-related changes. While clear separation emerges in later layers for subjects with AD, the overlap between NO and MCI profiles remains evident, reflecting the subtle and heterogeneous nature of early neurodegenerative alterations. This progressive refinement of embeddings highlights how DiGAN incrementally separates global structural patterns from localized disease-specific signals, offering interpretability and explaining why distinguishing NO from MCI is inherently more challenging than differentiating NO from AD.

Conclusion

In this paper, we present DiGAN, which integrates a latent diffusion model with an attention-based convolutional encoder for early detection of AD. By generating realistic longitudinal neuroimaging trajectories from limited training data, DiGAN addresses the scarcity and irregularity of clinical follow-ups and improves temporal continuity in disease modeling. Experiments on synthetic and ADNI datasets show that DiGAN consistently outperforms existing baselines, while providing interpretable embedding and attention maps that align with known neuroanatomical markers of early AD progression.

Table 2: Performance comparison of different models on synthetic and ADNI datasets for NO vs. MCI.

Datasets	Metrics	TVAE	LSCP	SUOD	GP	IsoForest	ALASCA	AnoGAN	DiGAN
Synthetic	Accuracy	0.825 \pm 0.055	0.433 \pm 0.024	0.408 \pm 0.044	0.835 \pm 0.043	0.496 \pm 0.031	0.450 \pm 0.028	0.522 \pm 0.064	0.948 \pm 0.016
	Sensitivity	0.919 \pm 0.083	0.000 \pm 0.000	0.121 \pm 0.123	0.765 \pm 0.083	0.289 \pm 0.095	0.110 \pm 0.074	0.320 \pm 0.072	0.998 \pm 0.004
	Specificity	0.732 \pm 0.036	0.866 \pm 0.027	0.700 \pm 0.121	0.908 \pm 0.024	0.704 \pm 0.059	0.787 \pm 0.039	0.730 \pm 0.103	0.896 \pm 0.031
	AUC	0.918 \pm 0.033	0.337 \pm 0.016	0.405 \pm 0.033	0.940 \pm 0.021	0.533 \pm 0.030	0.501 \pm 0.037	0.499 \pm 0.073	0.999 \pm 0.002
	Precision	0.773 \pm 0.035	0.000 \pm 0.000	0.213 \pm 0.186	0.891 \pm 0.034	0.486 \pm 0.091	0.303 \pm 0.160	0.551 \pm 0.105	0.907 \pm 0.022
	F1-score	0.839 \pm 0.052	0.000 \pm 0.000	0.149 \pm 0.137	0.820 \pm 0.052	0.357 \pm 0.090	0.159 \pm 0.100	0.398 \pm 0.068	0.950 \pm 0.014
ADNI	Accuracy	0.640 \pm 0.057	0.652 \pm 0.050	0.630 \pm 0.055	0.552 \pm 0.120	0.618 \pm 0.050	0.449 \pm 0.017	0.618 \pm 0.046	0.710 \pm 0.042
	Sensitivity	0.485 \pm 0.094	0.244 \pm 0.108	0.196 \pm 0.111	0.465 \pm 0.063	0.220 \pm 0.143	0.952 \pm 0.041	0.172 \pm 0.088	0.530 \pm 0.026
	Specificity	0.771 \pm 0.096	0.942 \pm 0.001	0.927 \pm 0.021	0.625 \pm 0.165	0.958 \pm 0.036	0.021 \pm 0.036	0.869 \pm 0.056	0.960 \pm 0.002
	AUC	0.643 \pm 0.025	0.572 \pm 0.105	0.578 \pm 0.103	0.520 \pm 0.162	0.575 \pm 0.095	0.495 \pm 0.099	0.574 \pm 0.096	0.700 \pm 0.000
	Precision	0.650 \pm 0.115	0.967 \pm 0.012	0.906 \pm 0.005	0.530 \pm 0.148	0.861 \pm 0.127	0.454 \pm 0.009	0.889 \pm 0.008	0.920 \pm 0.071
	F1-score	0.552 \pm 0.085	0.384 \pm 0.138	0.318 \pm 0.163	0.494 \pm 0.100	0.329 \pm 0.185	0.614 \pm 0.008	0.287 \pm 0.134	0.690 \pm 0.016

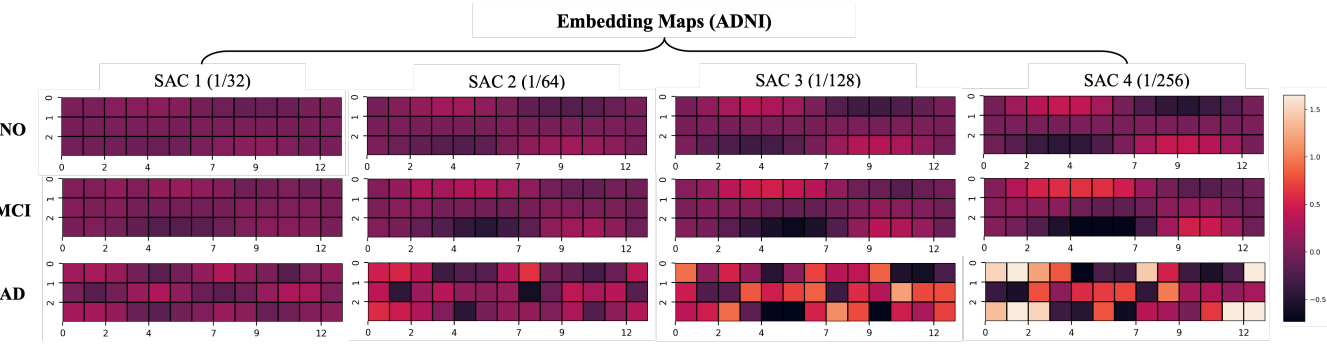


Figure 6: Embedding maps extracted from SAC units of DiGAN on the ADNI dataset. Each map shows the learned structural–temporal embeddings across subsequences.

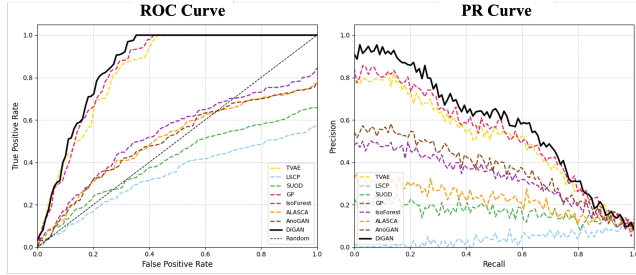


Figure 7: ROC and PR curves comparing the DiGAN performance for NO vs. MCI (synthetic).

Acknowledgments

We are thankful to Gabriel Ziegler (DZNE) for providing access to the synthetic dataset and for his valuable feedback throughout this study.

References

Alzheimer. 2024. 2024 Alzheimer’s disease facts and figures. *Alzheimer’s & Dementia: The Journal of the Alzheimer’s Association*, 20(5): 3708–3821.

Di Meco, A.; and Vassar, R. 2021. Early detection and personalized medicine: Future strategies against Alzheimer’s disease. In *Progress in Molecular Biology and Translational Science*, volume 177, 157–173. Elsevier.

Hyun, J. W.; Li, Y.; Huang, C.; Styner, M.; Lin, W.; Zhu, H.; and Initiative, A. D. N. 2016. STGP: Spatio-temporal Gaussian process models for longitudinal neuroimaging data. *NeuroImage*, 134: 550–562.

Jessen, F.; Wolfsgruber, S.; Wiese, B.; Bickel, H.; Mösch, E.; Kaduszkiewicz, H.; Pentzek, M.; Riedel-Heller, S. G.; Luck, T.; Fuchs, A.; et al. 2018. Design and first baseline data of the DZNE multicenter observational study on predementia Alzheimer’s disease (DELCODE). *Alzheimer’s Research & Therapy*, 10(1): 15.

Liu, F. T.; Ting, K. M.; and Zhou, Z.-H. 2008. Isolation Forest. In *2008 Eighth IEEE International Conference on Data Mining (ICDM)*, 413–422. IEEE.

Petersen, R. C.; Aisen, P. S.; Beckett, L. A.; Donohue, M. C.; Gamst, A.; Harvey, D. J.; Jack, C. R.; Jagust, W. J.; Shaw, L. M.; Toga, A. W.; Trojanowski, J. Q.; and Weiner, M. W. 2010. Alzheimer’s Disease Neuroimaging Initiative (ADNI): Clinical characterization. *Alzheimer’s & Dementia*, 6(3): 239–246.

Rahman, M. R.; Abdel Khaliq, L.; Piper, T.; Geyer, H.; Equey, T.; Baume, N.; Aikin, R.; and Maass, W. 2024. SACNN: Self Attention-based Convolutional Neural Network for Fraudulent Behaviour Detection in Sports. In *Proceedings of the Thirty-Third International Joint Conference on Artificial Intelligence (IJCAI-24)*, 6017–6025. International Joint Conferences on Artificial Intelligence.

Rombach, R.; Blattmann, A.; Lorenz, D.; Esser, P.; and Ommer, B. 2022. High-Resolution Image Synthesis with Latent

Diffusion Models. In *Proceedings of the IEEE/CVF Conference on Computer Vision and Pattern Recognition (CVPR)*, 10684–10695.

Schlegl, T.; Seeböck, P.; Waldstein, S. M.; Schmidt-Erfurth, U.; and Langs, G. 2017. Unsupervised Anomaly Detection with Generative Adversarial Networks to Guide Marker Discovery. In *Information Processing in Medical Imaging*, 146–157. Cham: Springer International Publishing.

Truter, N.; Jansen van Rensburg, Z.; Oudrhiri, R.; Van Niekerk, D. D.; Loos, B.; Singh, R.; and Louw, C. 2022. ALaSCA: a computational platform for quantifying the effect of proteins using Pearlian causal inference, with an example application in Alzheimer’s disease. *bioRxiv*, 2022–10.

WHO. 2017. Dementia: number of people affected to triple in next 30 years. News release. Geneva.

Zhang, J.; Zhang, Y.; Wang, J.; et al. 2024a. Recent advances in Alzheimer’s disease: mechanisms, clinical trials and new drug development strategies. *Signal Transduction and Targeted Therapy*, 9(1): 211.

Zhang, X.; Xu, S.; Chen, H.; Chen, Z.; Zhuang, F.; Xiong, H.; and Yu, D. 2024b. Rethinking Robust Multivariate Time Series Anomaly Detection: A Hierarchical Spatio-Temporal Variational Perspective. *IEEE Transactions on Knowledge and Data Engineering*.

Zhao, Y.; Hu, X.; Cheng, C.; Wan, C.; Wang, W.; Yang, J.; Bai, H.; Li, Z.; Xiao, C.; Wang, Y.; Qiao, Z.; Sun, J.; and Akoglu, L. 2021. SUOD: Accelerating Large-scale Unsupervised Heterogeneous Outlier Detection. In *Proceedings of Machine Learning and Systems*.

Zhao, Y.; Nasrullah, Z.; Hryniwicki, M. K.; and Li, Z. 2019. LSCP: Locally Selective Combination in Parallel Outlier Ensembles. In *Proceedings of the 2019 SIAM International Conference on Data Mining, SDM 2019*, 585–593.